A physically based 3-D model of ice cliff evolution over debris-covered glaciers

Pascal Buri[1], Evan S. Miles[2], Jakob F. Steiner[1], Walter W. Immerzeel[3], Patrick Wagnon[4,5], and Francesca Pellicciotti[6]

[1]Institute of Environmental Engineering, ETH Zürich, Zürich, Switzerland, [2]Scott Polar Research Institute, University of Cambridge, Cambridge, UK, [3]Department of Physical Geography, Utrecht University, Utrecht, Netherlands, [4]Université Grenoble Alpes, CNRS, IRD, LTHE, Grenoble, France, [5]International Centre for Integrated Mountain Development, Kathmandu, Nepal, [6]Department of Geography, Northumbria University, Newcastle upon Tyne, UK

Abstract We use high-resolution digital elevation models (DEMs) from unmanned aerial vehicle (UAV) surveys to document the evolution of four ice cliffs on the debris-covered tongue of Lirung Glacier, Nepal, over one ablation season. Observations show that out of four cliffs, three different patterns of evolution emerge: (i) reclining cliffs that flatten during the ablation season; (ii) stable cliffs that maintain a self-similar geometry; and (iii) growing cliffs, expanding laterally. We use the insights from this unique data set to develop a 3-D model of cliff backwasting and evolution that is validated against observations and an independent data set of volume losses. The model includes ablation at the cliff surface driven by energy exchange with the atmosphere, reburial of cliff cells by surrounding debris, and the effect of adjacent ponds. The cliff geometry is updated monthly to account for the modifications induced by each of those processes. Model results indicate that a major factor affecting the survival of steep cliffs is the coupling with ponded water at its base, which prevents progressive flattening and possible disappearance of a cliff. The radial growth observed at one cliff is explained by higher receipts of longwave and shortwave radiation, calculated taking into account atmospheric fluxes, shading, and the emission of longwave radiation from debris surfaces. The model is a clear step forward compared to existing static approaches that calculate atmospheric melt over an invariant cliff geometry and can be used for long-term simulations of cliff evolution and to test existing hypotheses about cliffs' survival.

1. Introduction

Debris covers 9–16% of the total glacier surface in the Hindu Kush-Karakoram-Himalaya region [*Kääb et al.*, 2012], a region where glaciers have undergone mass loss and shrinkage in area during recent decades [e.g., *Bolch et al.*, 2012; *Cogley*, 2016]. Patterns of glacier changes are heterogeneous and controlled by both climate and the varying magnitude and characteristics of debris mantles [*Kääb et al.*, 2012; *Scherler et al.*, 2011]. Sustained negative glacier mass balances result in higher relative debris cover, through increased exposure of debris due to the lack of substituting accumulation as well as additional deposits from destabilized moraines or valley flanks [e.g., *Kirkbride and Deline*, 2013; *Herreid et al.*, 2015], and it is expected that continued mass losses would lead to an increase in debris cover and thickness [*Herreid et al.*, 2015].

While the effect of a homogeneous layer of debris on the melt of the underlying ice is understood in theory [*Østrem*, 1959], the general behavior of debris-covered glaciers is much less well understood [*Ragettli et al.*, 2016]. A supraglacial debris mantle exceeding a few centimeters in thickness reduces the ablation of the underlying ice through reduced absorption of incoming solar radiation and longer distances for conductive heat [*Østrem*, 1959; *Nicholson and Benn*, 2006; *Evatt et al.*, 2015]. Nevertheless, recent studies have suggested that thinning rates on debris-covered glacier tongues are similar in magnitude to those of clean ice glaciers [*Gardelle et al.*, 2012; *Kääb et al.*, 2012], even when comparing equal elevation ranges [*Gardelle et al.*, 2013]. The issue remains controversial, as evidence has been provided by large-scale studies based on satellite images, while more detailed studies at the catchment scale have provided no support for similar thinning rates [*Ragettli et al.*, 2016]. It is, however, clear that a strong local increase in glacier ablation is associated with both supraglacial ponds [*Sakai et al.*, 2000; *Miles et al.*, 2016] and cliffs [*Thompson et al.*, 2016] forming on the debris-covered tongues of many Himalayan glaciers.

Supraglacial ice cliffs affect the surface evolution, glacier downwasting, and mass balance of debris-covered glaciers [*Inoue and Yoshida*, 1980; *Sakai et al.*, 1998; *Purdie and Fitzharris*, 1999; *Benn et al.*, 2012; *Pellicciotti et al.*, 2015; *Ragettli et al.*, 2016] by providing a direct ice-atmosphere interface, with low albedo because of the dust from the debris slopes, and exposure to high emissions of longwave radiation from the surrounding debris-covered surfaces [*Steiner et al.*, 2015; *Buri et al.*, 2016]. As a result, melt rates can be very high and ice cliffs may account for a significant portion of the total glacier mass loss [*Buri et al.*, 2016; *Thompson et al.*, 2016]. However, their contribution to glacier mass balance has rarely been quantified through physically based models. Melt on supraglacial ice cliffs has been investigated on Lirung Glacier (Himalaya, Nepal [*Sakai et al.*, 1998; *Steiner et al.*, 2015]), Koxkar Glacier (Tian Shan, China [*Han et al.*, 2010]), and Glacier du Miage (European Alps, Italy [*Reid and Brock*, 2014]), but the energy balance models used in those studies are point-scale models which calculate energy fluxes at individual cliff locations. Results from the only grid-based model to date accurately reflect energy fluxes and short-term cliff melt but are based on a static cliff geometry [*Buri et al.*, 2016]. While the surface energy balance and its variability in space was correctly reproduced by the model, applying that forcing only (without considering other processes affecting cliff evolution) on an unchanged cliff geometry would lead to the demise and disappearance of most cliffs. This is a perspective that seems unrealistic, although very few studies have extensively documented the evolution, formation, and survival cycle of cliffs [*Brun et al.*, 2016]. From a multitemporal data set of cliff topography and backwasting derived from structure-from-motion analysis (SfM) of high-resolution terrestrial and aerial photography on Lirung Glacier, it was apparent that cliffs exhibit a range of behaviors but mostly did not rapidly disappear [*Brun et al.*, 2016].

In this study, we use a unique data set of cliff geometry observations to document distinct patterns of cliff evolution including disappearance, growth, and stability, which cannot be explained satisfactorily by atmospheric melt alone. We then use the observations to improve the grid-based energy balance model described in *Buri et al.* [2016] through inclusion of periodic updates of the cliff geometry based on modeled melt. We also include the effect of adjacent supraglacial ponds and ice reburial from marginal debris.

Our main aims in doing so are (1) to document the evolution of a set of ice cliffs through analysis of rare, high-resolution field observations of cliff outlines and slope patterns, in order to understand the main processes that control the observed evolution and (2) to incorporate these processes into a dynamic model that can be used to (i) quantify the relative importance of those effects and (ii) simulate cliff evolution over seasonal and annual scales. We apply the new model to simulate cliff evolution over one Himalayan glacier during one melt season to determine the new cliff positions, horizontal and vertical extents, and mean slope and aspect values. Although operating with a data set of only four cliffs from a single study site, this work sheds light on mechanisms of cliff changes by quantifying them for the first time with a physically based, dynamic 3-D model, representing many of the key processes controlling ice cliff evolution.

2. Study Site and Data

We investigate four ice cliffs on the debris-covered Lirung Glacier in the upper Langtang Valley, Nepalese Himalaya (28.232°N, 85.562°E; Figure 1), using aerial and terrestrial surveys of cliff geometry at the beginning and the end of the ablation season, which in this monsoon-dominated area approximately corresponds to the monsoon season. The cliffs, indicated as cliffs 1–4, range between ∼4060 and 4200 m above sea level (asl) on the lower tongue of Lirung Glacier (Figure 1).

Two sets of high-resolution orthoimages and DEMs from UAVs were produced by SfM photogrammetry, covering the lower part of Lirung Glacier [*Immerzeel et al.*, 2014]. The two UAV-DEMs from 19 May and 22 October 2013 were originally produced at 0.2 m resolution and aggregated to 0.6 m because of the model's computational costs and numerical stability. They were used to derive the initial and final topography of the cliffs and the surrounding glacier surface, respectively. Selected UAV-DEM raster cells near cliffs 2 and 4 had unrealistic increased elevations due to water surface reflection in the May observations and were corrected manually by considering the local slope.

The outlines of the cliffs and nearby ponds were manually digitized from the UAV orthoimages, which have a spatial resolution of 0.1 m. Elevation models based on a triangulated irregular network (TIN) derived from UAV photogrammetry [*Brun et al.*, 2016] are used for validation of modeled volume losses.

An Automatic Weather Station (AWS) located on the tongue of Lirung Glacier (AWS Lirung, 4076 m asl, Figure 1) recorded the following meteorological variables, used as input to the ablation model: incoming shortwave
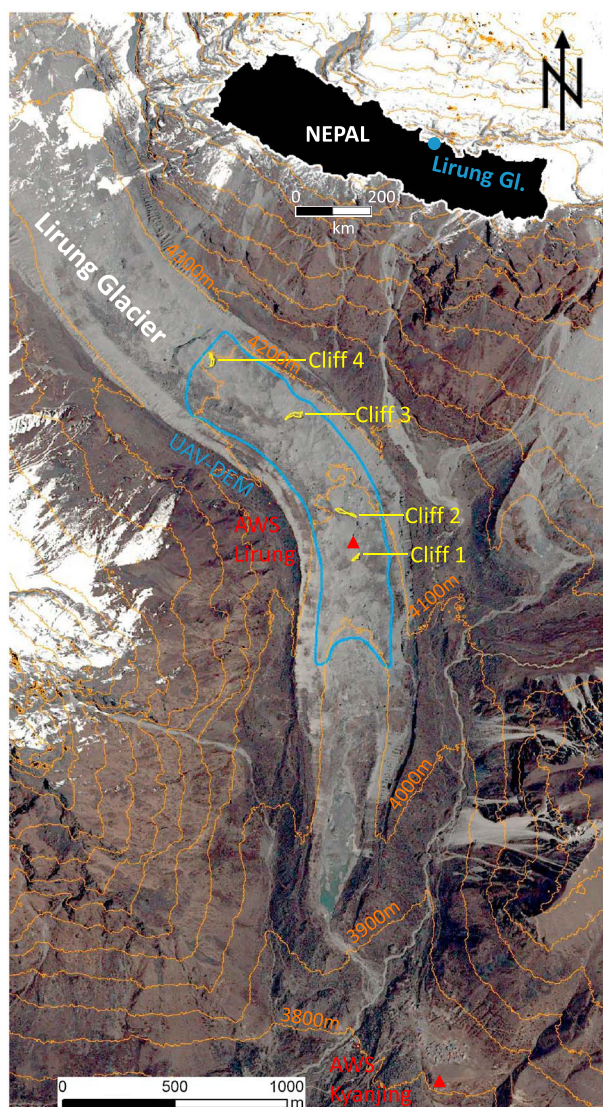
Figure 1. Overview of the tongue of Lirung Glacier, in the upper Langtang Valley, Central Nepalese Himalayas, based on a SPOT6-orthoimage from April 2014. The May UAV-DEM coverage is indicated in blue and the four investigated cliffs in yellow. The AWS sites are marked by a red triangle.

radiation (perpendicular to the surface), relative humidity of the air, wind speed, and air temperature (shielded and ventilated), all at a screen level of 2 m. Details about the sensor setup are provided in *Steiner et al.* [2015]. Debris surface temperature was measured, shielded from sunlight, on a rock at the station [*Steiner and Pellicciotti*, 2016]. Incoming longwave radiation was not measured at the AWS on the glacier and was therefore modeled with data from an AWS in Kyanjing (3857 m asl) about 2 km south of Cliff 1 (see Figure 1), following *Steiner et al.* [2015] and *Buri et al.* [2016]. Details of the modeling approach are provided in *Steiner et al.* [2015].

Some of the parameters used in the energy balance calculations are difficult to measure in the field (albedo for ice and debris, as well as surface roughness length) and were optimized in *Steiner et al.* [2015] and used as described in *Buri et al.* [2016]. These parameters were assumed to be uniform across the cliffs and constant in time.

3. Field Observations of Cliff Changes

The purpose of this section is to describe the cliff observations as documented by the UAV and field investigations, to detect patterns of changes between the beginning and end of the monsoon ablation season, and to infer the processes that may be important to the modeling of their evolution. We investigate the slope and
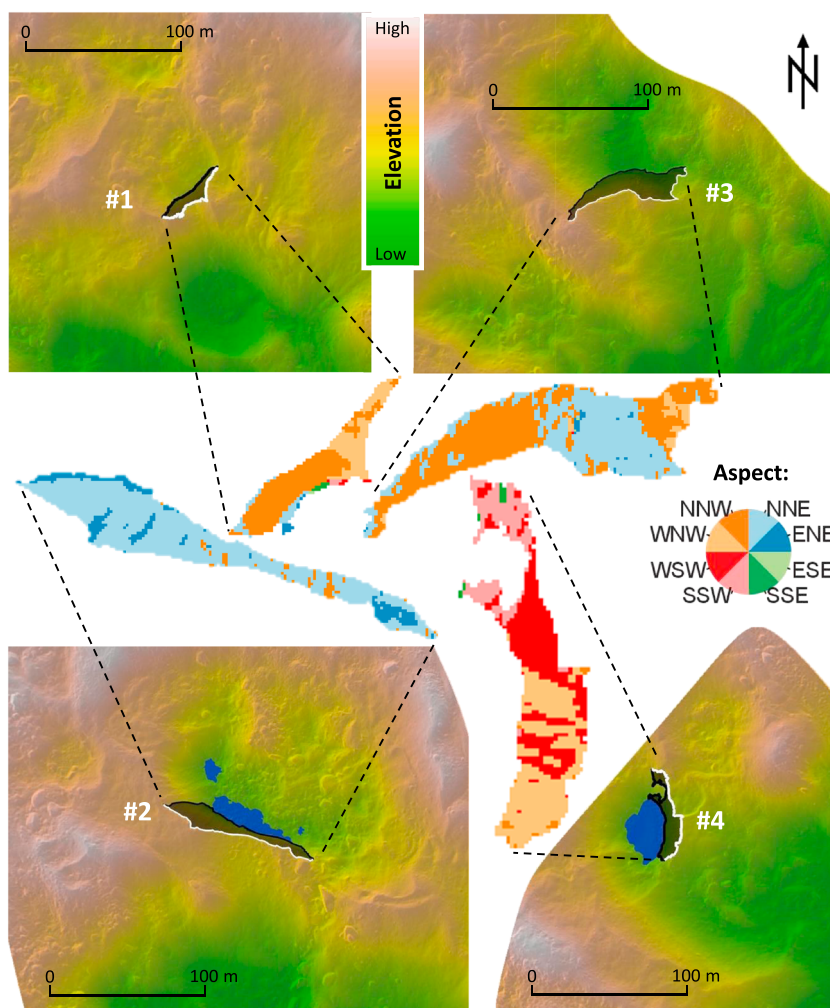
Figure 2. Aspect (insets) and elevation within 200 m × 200 m area of interest (maps) for each cliff (1–4) based on the May 2013 UAV-DEM. On the maps the two-dimensional shape of the cliffs (dark area) is indicated by lines, with the white line marking the crest of the cliffs and the black line their base. Blue areas indicate ponds (pond at Cliff 3 not visible due to small size). The map background shows colors relative to elevation topped by hillshade.

aspect distribution and the cliff areas and dimensions (Figures 2 and 3 and Table 1) in May and October as derived from the high-resolution UAV-DEM for the four cliffs. We then use them to identify different cliff types in terms of geometry and evolution.

3.1. Reclining Cliffs
Cliff 1 is the smallest of the four surveyed cliffs and presented steep slopes at its base in May 2013 (Figure 3). No pond was present in May 2013 (Figure 2), although the steep lower section (see slope and orthoimage in Figure 3) indicates a probable former pond connection which likely disappeared before the field visit and the UAV flights in May 2013 [Brun et al., 2016]. A small adjacent pond could be identified on two Google Earth satellite images from postmonsoon 2011 (27 September and 5 October, respectively), in contact with the cliff section showing the steepest slopes in May 2013.

Cliff 1 reclined during the 2013 monsoon season, as indicated by markedly lower slope values, especially at the cliff base (Figure 3 and Table 1). Its area slightly diminished (Table 1) and shape changed (Figure 3), but the more striking transformation is the flattening of slopes.

A small supraglacial water body, probably only fed by surface melt water, was in contact with Cliff 3 in May but not evident in October. A pattern of slope decline is evident for Cliff 3, similar to the pattern observed at Cliff 1 (Figure 3), with the steep slope section at the cliff's base minimized by October, also suggesting that the pond
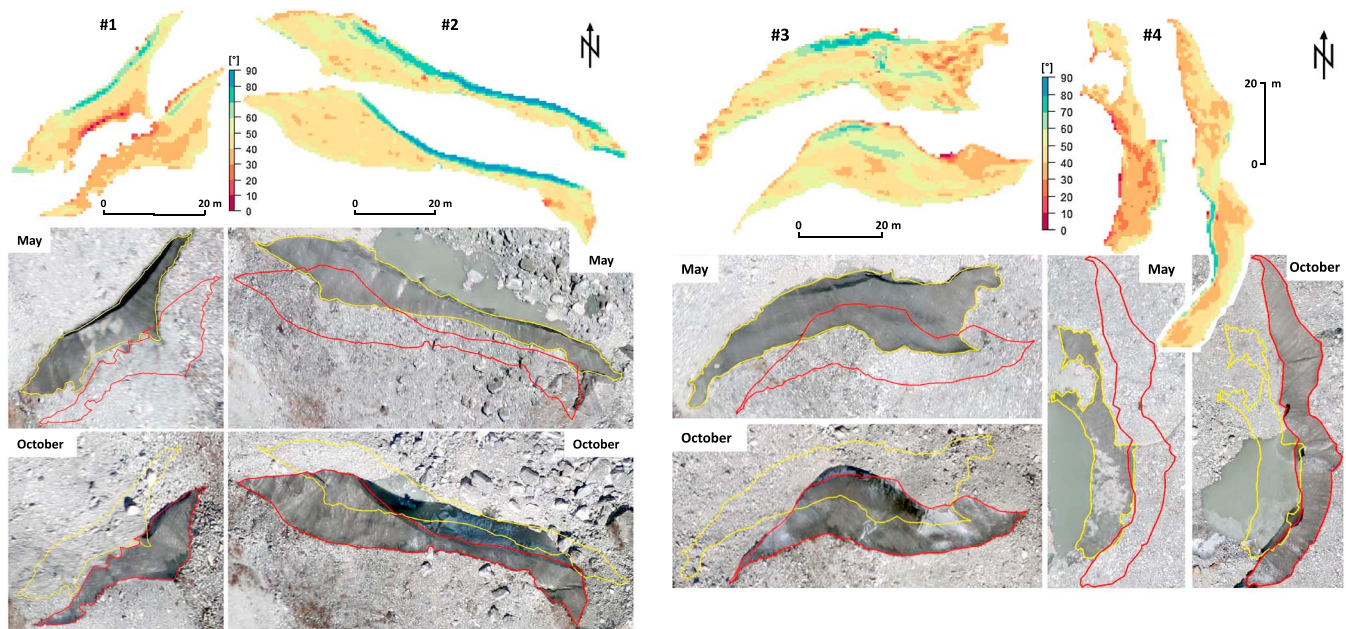
Figure 3. Slopes derived from the UAV-DEM and manually delineated outlines of the four cliffs in May (top or left raster; yellow line on orthoimage) and October (bottom or right raster; red line on orthoimage) 2013, used as initial conditions for the model. Note the different scale bars for different cliffs.

played a negligible role. The area of the cliff decreases slightly (Table 1). Cliff 3 is the only cliff which slightly alters its main orientation between May and October, from overall NNW aspect to predominant NNE (Table 1).

The flattening of both Cliffs 1 and 3 is not entirely apparent from comparison of their mean slopes between May and October, as changes in area also play a role in the averaging of single cell slopes into a mean cliff value. A clearer signal of the general reclining can be found in the reduction of the cliffs' vertical extent (Table 1) by 25.5% (Cliff 1) and 16.9% (Cliff 3). Both cliffs show a decreased inclined area in October, as a consequence of the removal of steep sections from the cliffs' bases. Additionally, the slopes behind the two cliffs in the direction of backwasting are characterized by a depression downglacier (Figure 2) so that the cliff's top ridge is lowered as a result of reduced ice volume for backwasting [*Brun et al.*, 2016]. This leads to a slope reduction at the upper portion of the cliff that progressively decreases the cliff area.

3.2. Persistent Cliffs

Cliff 2, the largest of the four cliffs, maintains a remarkably consistent area and self-similar geometry from May to October (Table 1 and Figure 3). Adjacent to the main section of the cliff a pond is present both in May and in October 2013 (see Figure 3).

The decrease in mean slope toward October is due to the slight flattening of a steep section at the eastern top part. Through the fall of a large boulder the shading of the uppermost cliff part was stopped at one point in the period between the observations. The vertical extent is very similar between May and October, further suggesting that the cliff geometry has remained self-similar while backwasting (Table 1 and Figure 11).

Table 1. Cliff Characteristics Derived From the UAV-DEM and Orthoimage, Shown as Mean Values for 18 May and 22 October 2013, Respectively[a]

Cliff #	Elevation (m asl)		Aspect (deg)		Slope (deg)		Vertical Extent (m)		Horizontal Extent (m)		Area (m²)	
	May	Oct	May	Oct	May	Oct	May	Oct	May	Oct	May	Oct
1	4066.4	4061.7	328.3 (NNW)	316.9 (NNW)	46.8	43.5	14.5	10.8	47.4	46.1	297.5	251.8
2	4092.2	4092.2	29.8 (NNE)	31.8 (NNE)	53.0	48.4	23.7	24.7	100.7	95.6	1107.9	1113.3
3	4161.2	4155.5	358.9 (NNW)	3.1 (NNE)	49.7	48.5	33.1	27.5	82.3	72.6	1303.6	990.9
4	4201.5	4204.7	263.7 (WSW)	258.8 (WSW)	42.2	44.0	14.7	23.7	60.4	82.4	505.0	757.8

[a]For elevation, the maximum value within each cliff area is taken. Aspect is defined from 0 to 360°, with north at 0° (vectorial mean). Values of vertical extent indicate the highest difference in elevation within the cliff area; horizontal extent is the manually defined maximum straight distance within the cliff outline. The area represents the real inclined area, calculated considering cell resolution and slope.

The backwasting pattern is uniform, and we know from water level records that the pond first filled slightly and then drained gradually.

3.3. Expanding Cliff

Cliff 4 is the only cliff which increases noticeably in area between the two observations (Table 1 and Figure 3), mainly due to its initial negative planform curvature in May 2013 (see aspect in Figure 2). Both vertical and horizontal extents increase in a pronounced manner from May to October, by 61.2% and 36.4%, respectively (Table 1). Slopes at the base of the cliff become steeper (Figure 3d), and the average slope increases by 1.8° (Table 1).

Although a pond is in contact with the cliff in both May and October, the cliff shape changes markedly during the melt season as a result of the draining of the pond, which lowers by about 6 m (calculated as a net change in elevation between the two DEMs). In addition to the increase in area, the most striking change in the geometry of this cliff is the reversal of slope patterns: the base of the cliff in contact with the water has generally shallow slopes in May, while in October the cliff zones at the pond shore are the steepest. In May, on the other hand, the steepest sections were located at the top of the cliff, in its central section. It is possible that steep slopes at the base were also present in May but covered by the higher pond level and became exposed in October with the lowering of the water level.

3.4. Summary of Observed Cliff Types

To summarize, three categories of cliff behavior can be identified in terms of geometry, evolution, and pond coupling:

1. Absence of pond contact permits flattening of the cliff and causes continuous cliff reclining.
2. Consistent pond presence leads to steep sections at the cliff base, enabling a stable cliff geometry.
3. Lowering pond water level reveals steep formerly submerged ice in a cliff that grew radially in size.

Due to our restricted sample size, these cliff types might not be representative of the full variety observed at larger scales, on different glaciers, or in distinct climatic regimes. Assessing the dominant processes and changes for a larger sample of cliffs and for different locations will be a necessary future step for understanding the dynamics and relevance of ice cliffs.

4. Modeling Cliff Evolution

The patterns of cliff evolution observed on Lirung Glacier and described in section 3 cannot be explained by considering a static cliff geometry and by applying atmospheric melt alone [*Buri et al.*, 2016]. From field evidence and qualitative results from the pioneering early studies on debris-covered glaciers in the Himalaya [e.g., *Iwata et al.*, 1980; *Sakai et al.*, 1998], as well as from results of very recent works, it is evident that cliffs are moderated by the presence of supraglacial ponds at their base [*Röhl*, 2008; *Miles et al.*, 2016]. Ponds were also observed to affect retreat of ice-cored moraines located at glacier termini in St. Elias Mountains (Canada) and in Vestfold Hills (Antarctica) [e.g., *Driscoll*, 1980; *Watson*, 1980; *Pickard*, 1983]. Field observations suggest that ice reburial by debris can considerably affect cliff geometry and area [*Thompson et al.*, 2016]. The inaccuracy of the static approach is exemplified by calculating only melt due to the interaction with the atmosphere (Figure 4). With the grid-based model that considers a static geometry where the cliff geometry is only updated once at the end of the melt season (hereafter referred to in short as "static model" and indicated as "S Model" [*Buri et al.*, 2016]), the patterns of aspect (Figure 4a) and slope (Figure 4b) after one melt season are not realistic. This is mainly due to the long period before an update to geometry and hence long melt vectors that can intersect each other. Along with evidence from the field, this prompted the development of the new model presented here, which is dynamic in the sense that regular updates of the cliff geometry are conducted on the base of the high-resolution ablation calculations. We also represent two key processes observed in the field that seemed to affect cliff geometry and dynamics: (a) the presence of ponds and (b) reburial of lateral cliff sections by adjacent debris.

4.1. Model

With this dynamic approach (hereafter called "D Model") we simulate cliff evolution by updating the cliff shape in three dimensions considering melt, surface geometry, adjacent ponds, and debris slopes. The energy balance equation is solved at an hourly time step; all other model steps are performed at monthly intervals. A monthly time step was chosen as a compromise between the computational costs and the need to calculate melt vectors compatible with the cell size.
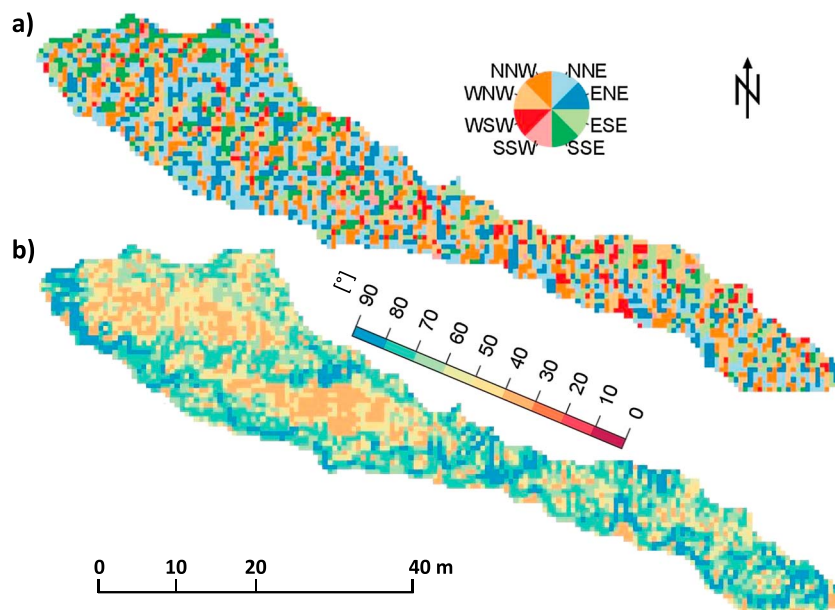
Figure 4. Modeled (S Model) (a) aspect and (b) slope for Cliff 2 for October 2013 without considering intermediate geometry updates but only a final melt translation resulting from energy exchange with the atmosphere at the end of the melt season.

A daily geometry update was unreasonable for two reasons: computational costs and a geometry update distance less than the grid size, as typical daily melt rates at the cliffs surface are at the order of $<10^{-1}$ m.

The model is coded in the open-source software R [*Core Team*, 2015] and is run separately for each cliff using the UAV-DEM of 0.6 m resolution. In the following, we explain the single modeling steps inside the D Model (Figure 5).

4.1.1. Cliff Outline Derivation (Step 1)

The outline of the ice cliff is needed as input to initialize the model, enabling separation of debris-covered and debris-free area in the calculations. Using the true-color georeferenced UAV orthoimage from May 2013,
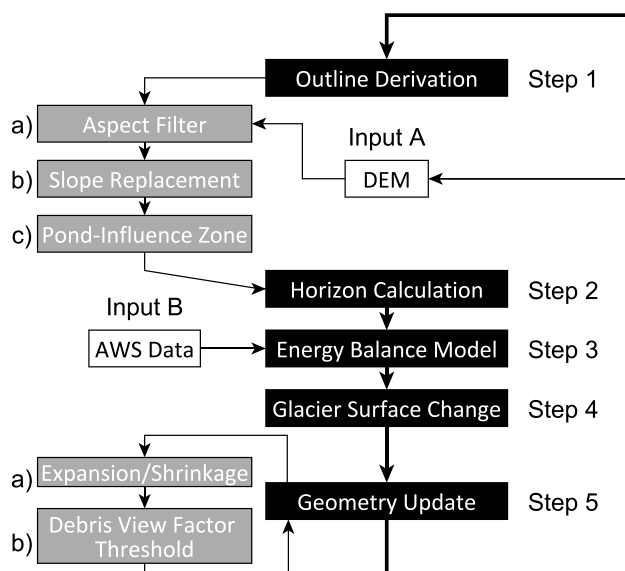

Figure 5. Modeling chain (steps 1 to 5) within the dynamic ice cliff backwasting model (D Model). Input A is for initialization of the UAV-DEM, subsequently the updated DEM based on step 5. Input B is the hourly time series of meteorological data.

supported by terrestrial photography and experience from the field visits, cliff and pond outlines are derived manually. The latter are used to identify the pond-affected zones of a cliff (step 1c).

After each geometry update (step 5, section 4.1.5) the new cliff polygon is derived automatically to run the model on the new geometry. As a result of the different aspects (and therefore melt directions) the application of the melt vectors to each cliff cell can lead to voids between the translated cliff raster. The term "melt vector" describes the melt distance in combination with the three-dimensional melt direction per cliff cell. To avoid gaps within the updated cliff, the new outline is based on a convex-hull approximation, the alpha shape method [*Edelsbrunner et al.*, 2006]. This approach draws a connected line around the updated cliff raster using a chain of circles approximating the cliff shape as closely as possible. The radius of the alpha shape circles is set to 3 times the resolution, i.e., 1.8 m. This size provides the best results in terms of penetrating into gaps between cells and not splitting the cliff into multiple polygons. The model internally increases this radius in case the cliff polygon is split, until a closed shape is reached again. In this way the model is avoiding dividing the cliff into multiple areas. As a consequence of the alpha shape method, the new cliff outline can increase in size compared to the previous polygon but can also shrink if transferred cells fall into the same cell after melting. Since these overlayed cells usually do not have the same elevation, a vertical discontinuity can occur with more than one elevation value per cell. If this happens, the minimum of the layered cell elevation values is taken and assigned to the cell.

In this study the DEM which is updated after model step 5 is referred to as the "active DEM." By masking it with the cliff polygon, the geometry of the cliff surface can be extracted. In the initial model run, the UAV-DEM from May 2013 serves as input, while in every subsequent interval the active DEM is used. Slope and aspect are derived for every cell together with its elevation from the active DEM based on the algorithm of *Horn* [1981] for rough topography using eight neighbors with differential weights and excluding the central cell itself. Marginal raster cells can be represented erroneously in terms of slope and aspect, as they can be influenced through the Horn algorithm by adjacent debris cells. To avoid these edge effects, we perform two steps (a and b below) to obtain a stable and realistic initial geometry for the ablation modeling.

Aspect filter (step 1a). A median filter with a window of size 9×9 cell (29.16 m^2) is applied to all aspect values within the cliff area in order to (1) remove lateral edge effects at the transition of ice to debris along the cliff outline and (2) smooth out the high aspect variability of the active DEM, which is partly due to small inaccuracies in steep terrain. The filter is needed to avoid calculation of an incorrect melt direction, as the melt vector depends partly on the aspect of a cliff cell.

Slope replacement (step 1b). A threshold of 40° is applied to distinguish between debris-covered (<40°) and potentially debris-free cells (≥40°). The threshold has been determined from field and satellite measurements by *Foster* [2010] on Miage Glacier. Although maximum angles at which loose material can remain on inclined ice surfaces might vary depending on thickness and shape of debris [*Reid and Brock*, 2014], ice-exposed slopes <40° were measured only rarely on supraglacial cliffs on the tongues of both Lirung [*Steiner et al.*, 2015] and Langtang Glacier in 2013 and 2014 (unpublished). Unrealistically low slopes on the cliff surface, which were apparent especially at the cliff edges, would produce steep melt vectors pointing downward almost vertically. To avoid this effect, all cliff cells below the slope threshold were set to 40°.

Pond influence zone (step 1c). The presence of supraglacial ponds seems to have an important effect on ice wall evolution [*Driscoll*, 1980; *Watson*, 1980; *Pickard*, 1983; *Miles et al.*, 2016; *Buri et al.*, 2016; *Brun et al.*, 2016]. Two horizontal buffers are applied to define a potential influence zone on the ice cliff surface. The first one is applied to search for all cliff raster cells lying within a 1 m band around the pond shore, while the second buffer identifies cliff cells with a slope ≥60° at a maximum distance of 5 m from the pond outline. The two resulting groups of cells are merged to a pond influence zone, where an enhanced melt rate is added to the horizontal melt component derived from the atmospheric energy balance (step 3). This extra melt accounts for subaqueous melt and is taken equal to 0.033 m d^{-1}. This is the mean value calculated by *Miles et al.* [2016] in their energy balance study of a pond (at Cliff 2) on Lirung Glacier during monsoon 2013. Calving, although observed at other field sites [e.g., *Inoue and Yoshida*, 1980], is unlikely to occur for these cliffs since the ponds are small [*Sakai et al.*, 2009].

4.1.2. Horizon Calculation (Step 2)

The horizon angles and viewing factors for each cliff cell are calculated as described in *Buri et al.* [2016]. To describe proximal and distal topography and determine view factors for each radiative flux, we use a combination of the active DEM (for proximal topography) and the ASTER-GDEM2 (Advanced Spaceborne Thermal

Emission and Reflection Radiometer global DEM 2) (for distal topography) with a resolution of 1 arc sec (~30 m) [*Tachikawa et al.*, 2011], following *Steiner et al.* [2015] and *Buri et al.* [2016]: the active DEM, adapted after each geometry update, is used to describe the close topography within a 200 by 200 m grid (Figure 2), while the ASTER-GDEM2 is used for the rest of the glacier surface and distant mountain ridges for calculation of shading [see *Buri et al.*, 2016, Figure 4]. Details of all calculations are provided in *Buri et al.* [2016].

4.1.3. Energy Balance (Step 3)

The view factors and horizon angles calculated in step 2 are used in the surface energy balance model for a fully distributed calculation of the radiative fluxes.

The energy balance at the cliff surface is

$$Q_m = I_n + L_n + H + \text{LE}, \tag{1}$$

where Q_m is the energy flux available for melt, I_n and L_n are the net shortwave and longwave radiation fluxes, H is sensible heat, and LE is latent heat flux. All fluxes are perpendicular to the surface and expressed in W m^{-2}. The heat from precipitation and conductive heat flux into the ice are neglected [*Reid and Brock*, 2014]. The surface energy balance for each cliff cell is computed using hourly meteorological data following *Buri et al.* [2016]. The model is run from 19 May to 22 October 2013 (dates of the UAV data acquisitions).

4.1.4. Glacier Surface Change (Step 4)

While ice cliffs backwaste several meters over a single melt season [*Brun et al.*, 2016], the debris-covered glacier surface also slowly changes due to subdebris melt and glacier flow. The relevant glacier dynamics are considered in the model by using tie points, which are detectable objects visible in both UAV orthoimages in May and October 2013. Large boulders serve as tie points and define stable references on the glacier during this period. Based on a distributed tie point approach [*Immerzeel et al.*, 2014], a thin plate spline interpolated map of displacement was created. Because the tracked boulders lie on the debris-covered parts of the glacier, the differential ablation occurring at ice cliffs does not affect the interpolation. The resulting map provides vertical and horizontal surface changes for every grid cell on the stable glacier surface. The vertical glacier change is applied to the active DEM together with the monthly cliff shape recalculation. The horizontal surface movement is not considered in the model but used to correct the observed October cliff outlines (Figure 8) for the glacier surface displacement from May to October 2013. Vertical and horizontal shifts are very small on Lirung Glacier with mean daily changes of −0.0049 and 0.0072 m d^{-1}, respectively.

4.1.5. Geometry Update (Step 5)

In the last model step the cliff geometry is updated according to the melt of ice per cliff cell, d_{melt} (m), resulting from the energy balance calculations in step 3 accumulated over each month:

$$d_{xy} = d_{\text{melt}} \sin\beta, \quad d_z = d_{\text{melt}} \cos\beta, \tag{2}$$

$$d_x = d_{xy} \sin\gamma, \quad d_y = d_{xy} \cos\gamma, \tag{3}$$

where d_z and d_{xy} (m) are the melt distances in vertical and horizontal directions, respectively. The latter is the resulting vector of the horizontal x and y components, d_x and d_y, respectively. The angles β and γ indicate slope and backazimuth (γ = azimuth −180°) of the cliff cell, respectively (Figure 6).

The new cliff raster cannot be simply embedded into the glacier-wide active DEM, as the updated cells are now located at a different position due to backwasting. The horizontal melt vectors are used to remove relict topography from the former cliff position. The elevation of the cells overlaid by the melt vectors were interpolated linearly between the starting and ending points of the melt vector.

Expansion and shrinkage. Internal and external buffers are applied to the cliff outline once the cliff cells are backwasted and the updated cliff is embedded into the active DEM. The width of both buffers is set to 1 m. Shallow cells in the internal buffer with slopes <40° are assumed to become debris covered in the next modeling step, consistent with the classification of debris-covered and debris-free surfaces in the outline derivation. The cells selected within the internal buffer allow the cliff to shrink. In the external buffer, steep cells ≥40° are detected. These are likely to be newly free of debris, and we include these in the new cliff area as a method of expansion. However, we exclude cells that were previously cliff cells but are now outside the cliff outline after applying the melt vectors. These are unlikely to contribute to expanding the cliff area, as the main melt direction in this border area is toward the new cliff and therefore in conflict with cliff expansion.
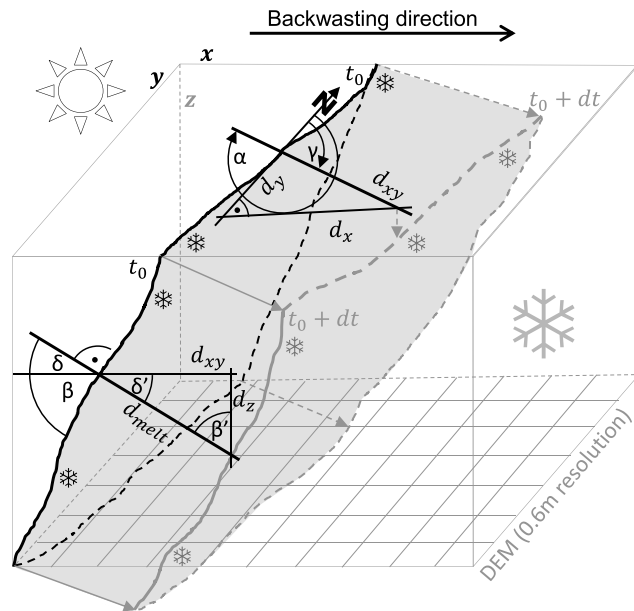
Figure 6. Schematic cross section of cliff backwasting from left to right (step 5). All cliff edges which are visible from the reader's point of view are shown as solid lines; hidden lines are dashed.

Debris view factor threshold. Unrealistic cliff outgrowths are limited in the model by the application of a sky view factor threshold. Lateral outgrowths of the cliff surface, unrealistically directed toward and cut into debris slopes, are often not automatically removed by the slope threshold described above. To contain these incorrect instances of expansion, cliff cells with high debris view factors ($V_d > 0.45$) are converted into debris-covered cells. The threshold is assumed to be equal for all cliffs and selected according to test runs with the most realistic results. V_d can be regarded here as a measure of how deep a cliff is cut into a debris ramp. Therefore, using V_d as a parameter to control cliff expansion has a clear physical meaning, as above the critical value the portion of debris seen by a cliff cell exceeds 45% of the total surrounding area (i.e., less than 55% is defined as sky or ice), which makes reburial by surrounding rocks or melt-out by extrahigh longwave
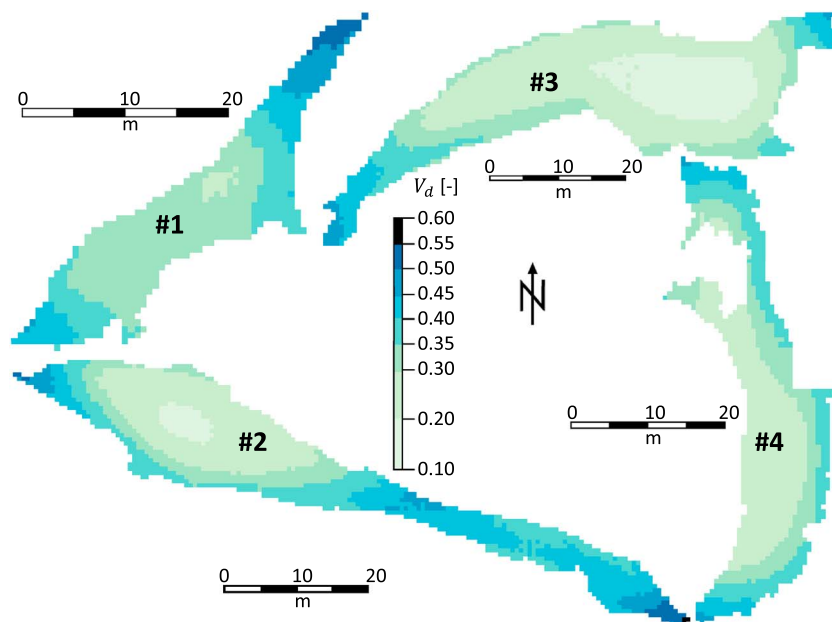

Figure 7. Modeled debris view factors (V_d) for each cliff (1–4) calculated from the initial UAV-DEM in May. Cliff cells with $V_d > 0.45$ are removed from the cliff area and converted into debris cells (model step 5b).

Table 2. Validation Metrics and Results of the Sensitivity Analysis for Different Model Runs (Listed in the First Column)[a]

Run	Tested Value	Recall	Precision	*F* score	Sensitivity
D Model		0.872 (0.139)	0.600 (0.068)	0.708 (0.086)	
Cliff 1		0.965	0.587	0.730	
Cliff 2		0.933	0.705	0.803	
Cliff 3		0.957	0.592	0.731	
Cliff 4		0.633	0.516	0.569	
S Model		0.807 (0.057)	0.480 (0.079)	0.599 (0.071)	
Cliff 1		0.726	0.382	0.501	
Cliff 2		0.846	0.600	0.702	
Cliff 3		0.873	0.448	0.592	
Cliff 4		0.784	0.488	0.602	
PondOff		0.874 (0.152)	0.587 (0.075)	0.699 (0.094)	
rs + 20 cm	80 cm	0.730 (0.141)	0.627 (0.122)	0.667 (0.104)	0.0006 ΔF/cm rs
ϵ_d − 2%	0.929	0.872 (0.137)	0.594 (0.082)	0.704 (0.086)	0.0026 ΔF/% ϵ_d
ϵ_d + 2%	0.967	0.875 (0.131)	0.578 (0.078)	0.693 (0.087)	
ϵ_i − 2%	0.959	0.876 (0.125)	0.581 (0.079)	0.698 (0.083)	0.0036 ΔF/% ϵ_i
ϵ_i + 2%	0.996	0.880 (0.124)	0.602 (0.074)	0.712 (0.082)	
β_T − 10%	36°	0.905 (0.086)	0.559 (0.077)	0.688 (0.068)	0.0001 ΔF/° β_T
β_T − 20%	32°	0.947 (0.029)	0.536 (0.082)	0.681 (0.065)	0.0001 ΔF/° β_T
β_T + 20%	48°	0.743 (0.208)	0.632 (0.112)	0.679 (0.153)	
V_{d_T} + 10%	0.495	0.881 (0.161)	0.533 (0.069)	0.661 (0.090)	0.0116 ΔF/% V_{d_T}
α_i − 20%	0.192	0.885 (0.132)	0.583 (0.088)	0.700 (0.090)	0.0001 ΔF/% α_i
α_i + 20%	0.288	0.874 (0.165)	0.583 (0.063)	0.698 (0.095)	
α_d − 20%	0.089	0.878 (0.139)	0.584 (0.082)	0.698 (0.085)	0.0000 ΔF/% α_d
α_d + 20%	0.134	0.873 (0.127)	0.584 (0.075)	0.697 (0.083)	

[a]The values are averaged over the four cliffs from May to October. For D and S Model runs the metrics for each cliff are shown additionally. Standard deviation among cliffs is shown in parentheses. Except for the S Model run, all runs are based on the D Model with a single parameter changed at a time. In run "PondOff" the pond influence algorithm was suppressed. In run "rs" the spatial resolution of the UAV-DEMs was altered, in ϵ_i and ϵ_d the emissivities of ice and debris, respectively, were changed. "β_T" and "V_{d_T}" indicate the runs where the threshold values for slope and debris view factor were modified, α_i and α_d the runs where ice and debris albedo were changed. The second column shows the value corresponding to each specific run. The metrics Recall, Precision, and *F* score are described in section 4.2. Sensitivity is shown as change in the *F* score (ΔF) per unit change of the corresponding parameter.

radiation likely. Figure 7 shows the distribution of V_d as modeled for the initial cliff shapes in May 2013. As described above, all cliff cells above the threshold are considered to be covered by debris by the end of each model interval and no volume loss is assigned to these areas.

4.2. Validation Metrics

We validate the model by comparing observed and modeled cliff dimensions, slopes, and aspects, as well as comparing the calculated volume losses to those derived from a TIN-based calculation in *Brun et al.* [2016]. Direct comparison of the observed and modeled area is not very meaningful, as the same single absolute surface area value could correspond to two different cliff shapes and locations. To take into account the areas that are correctly identified by the model, we calculate metrics that are commonly used in image classification and segmentation for binary images. We define three possible outcomes when identifying a cell as belonging to a cliff or not: (1) true positive (TP), when a cell is correctly detected as cliff by the model; (2) false positive (FP), when a cell is erroneously modeled as cliff; and (3) false negative (FN), when a cell is modeled as debris but in reality is part of a cliff. Using TP, FP, and FN, we then define the following common metrics [e.g., *Olson and Delen*, 2008; *Rittger et al.*, 2013]:

$$\text{Precision} = \frac{\text{TP}}{\text{TP} + \text{FP}}, \qquad (4)$$

Table 3. Cliff Characteristics Derived From the UAV-DEM ("Obs") and Modeled With the D Model ("Mod")[a]

	Elevation			Aspect			Slope			Vertical Extent			Horizontal Extent		
	(m asl)		(m)	(deg)		(deg)	(deg)		(%)	(m)		(%)	(m)		(%)
Cliff	Obs	Mod	Dev	Obs	Mod	Dev	Obs	Mod	Dev	Obs	Mod	Dev	Obs	Mod	Dev
1	4061.7	4062.9	1.2	320.2	323.2	3.0	42.0	43.9	4.6	10.8	11.6	6.8	46.1	47.6	3.3
2	4092.2	4093.2	1.0	28.2	30.9	2.7	56.5	51.0	−9.8	24.7	25.9	4.9	95.6	93.9	−1.8
3	4155.5	4161.8	6.3	2.9	0.2	2.7	49.0	46.2	−5.6	27.5	33.9	23.2	72.6	86.0	18.5
4	4204.7	4207.1	2.4	259.6	242.3	17.4	47.0	45.2	−3.9	23.7	23.8	0.4	82.4	80.3	−2.5

[a]The mean values are shown together with the respective deviations for 22 October 2013. For elevation the maximum value within the cliff area was taken. Aspect values (vectorial mean) are defined from 0 to 360° with north at 0°. Mean aspect and slope values are weighted with the inclined area of each cliff cell. Values for vertical extent indicate the highest difference in elevation within the cliff area; horizontal extent shows the manually defined maximum straight distance within the cliff outline.

$$\text{Recall} = \frac{\text{TP}}{\text{TP} + \text{FN}} \,, \tag{5}$$

$$F = 2 \cdot \frac{\text{Precision} \cdot \text{Recall}}{\text{Precision} + \text{Recall}} = \frac{2 \cdot \text{TP}}{2 \cdot \text{TP} + \text{FP} + \text{FN}} \,. \tag{6}$$

Precision measures the probability that a cell detected as cliff by the model indeed is cliff [*Rittger et al.*, 2013], and Recall is the fraction of real observed cliff area that was correctly detected in the model and shows the probability of detection [*Dong and Peters-Lidard*, 2010]. *F* (*F* score or Dice coefficient), a measure of segmentation agreement, balances Precision and Recall by penalizing both missing cliff cells and falsely detected debris as cliff [*Dice*, 1945; *Gilani and Rao*, 2009; *Rittger et al.*, 2013]. It ranges from 0, indicating no spatial overlap between two sets of binary segmentation results, to 1, indicating complete overlap [*Zou et al.*, 2004].

4.3. Model Sensitivity

Since several of the model parameters are evaluated on individual tests, by trial and error or taken from the literature, we perform a sensitivity analysis to evaluate their importance to the model outputs (Table 2). Assuming as reference the D Model run with the setup described in section 4, we vary each parameter one at a time by a given amount (chosen based on field experience or from the literature) and calculate the corresponding Recall, Precision, and *F* Score. We also evaluate the metrics for the S Model run and for a run where the pond influence is turned off. The varied parameters are spatial resolution of the UAV-DEMs, emissivities of ice and debris, threshold values of slope, and debris view factor, as well as ice and debris albedo.

We evaluate the sensitivity of the model to changes in the parameters by calculating the change in *F* score per change of parameter unit (i.e., degree or percentage).

5. Results

In this section we compare D Model results to the observed October surface. The S Model simulations are also presented for comparison. First we focus on cliff dimensions, slope, and aspect, then we investigate time series of radiative fluxes for each cliff and recorded meteorological data to explain differential patterns of cliff changes. Finally, the calculated volume loss and melt rates per cliff are compared to validation data and model sensitivities are briefly discussed.

5.1. Dimensions, Slope, and Aspect

The evolution of the four cliffs in terms of slope, aspect, and outline is shown in plan view in Figure 8 and as profile for Cliff 2 in Figure 11. Cliff geometry and dimensions, modeled and observed, are listed in Table 3.

5.1.1. Cliff 1

The geometry of Cliff 1 at the end of the monsoon season is reproduced well by the model. The initial steep section along a large part of the cliff base disappears, in agreement with observations, substituted by a shallower surface continuously sloping into the debris (Figure 8a). A small but distinct steep section in the cliff upper area is apparent in the simulations but not in the October UAV-DEM. The modeled average slope (43.9°) is 4.6% higher than observed (Table 3). The modeled vertical and horizontal dimensions show only a small deviation compared to the observations, with 6.8 and 3.3%, respectively (Table 3). The mean simulated aspect deviates by 3° toward north.
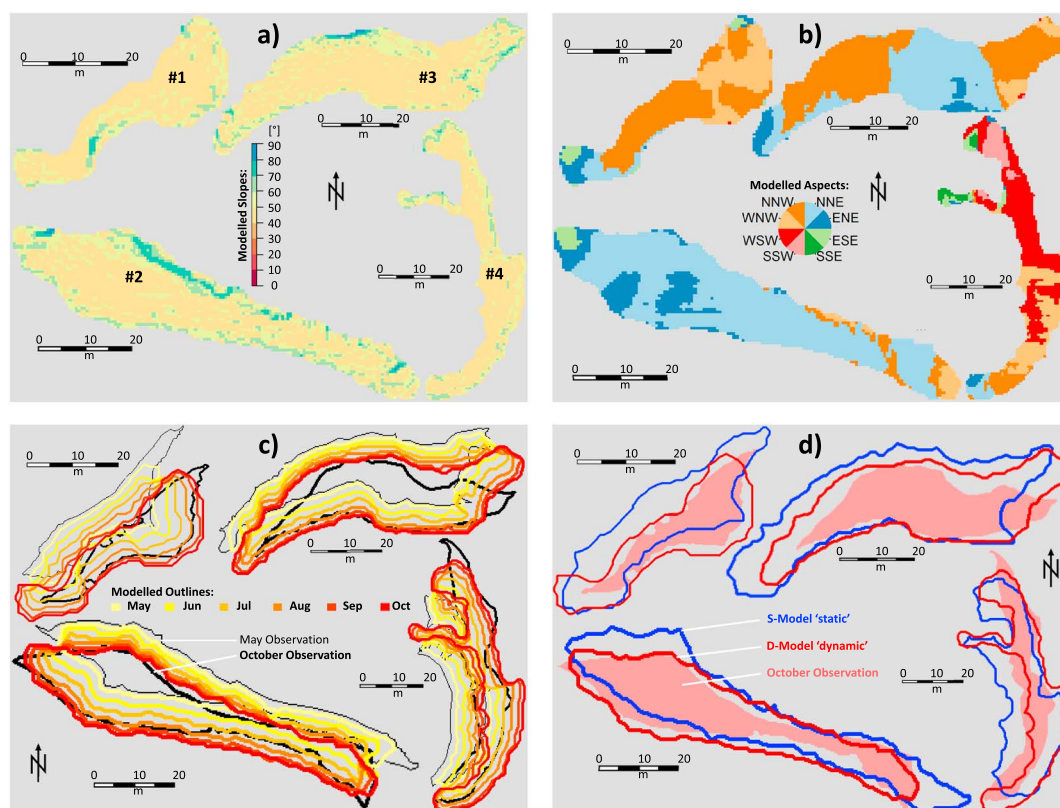
Figure 8. Model results of (a) slope and (b) aspect for October 2013 for each cliff (1–4). (c) The simulated cliff evolution based on the monthly updated outlines (D Model); for comparison the May and October observations are shown in the background. (d) The October cliff outlines simulated with the D Model (red) and the S Model (blue), respectively. The rose area in the background indicates the observed cliff area from the October UAV orthoimages.

The cliff outline, and the magnitude of the backwasting, is also reproduced well by the model with the exception of the lateral sections. The modeled outline along the top (south) and base (north) of the cliff agrees well with the observed shape, but the lateral margins are not accurately reproduced. The western corner sees a larger area than observed, whereas the eastern corner is partly removed (Figure 8a).

Comparison with the output of the S Model (Figure 8d) shows that for this cliff it is crucial to account for the dynamic processes included in the D Model, and the S Model is not able to reproduce the position of the cliff base, with less backwasting at the base but also an overestimation of the cliff area in its topmost sections.

5.1.2. Cliff 2

The agreement between modeled and observed geometry is very good for Cliff 2, and the self-similarity of the May and October geometry (Figures 3) is reproduced well by the model in terms of outline and slope distribution (Figures 8 and 11). The steep lower section, a principal characteristic of Cliff 2 in both May and October, is present also in the modeled cliff shape, even though some discrepancies are evident. The D Model simulates the average slope (51°) with a deviation of −5.5° or 9.8%, the highest among all cliffs. The modeled cliff dimensions agree very well, with a small discrepancy of 1.2 m (vertical) and −1.7 m (horizontal). The average modeled aspect agrees with the average observed aspect (with a difference toward east of 2.7°).

The average backwasting is well reproduced, and the cliff base and its top are simulated in the correct location. This is apparent also for the S Model in the central section of the cliff, but a main deficiency when using the S Model is a distinct outgrowth of ice at the eastern margin and a similar remnant in the northwestern section.

5.1.3. Cliff 3

The slope distribution at Cliff 3 was relatively homogenous in premonsoon and postmonsoon, with a distinct steep part at the central base section which implied the presence of a pond for some period, despite the fact that in May 2013 only a very small frozen pond was observed (Figure 3). The conservation of the slope pattern
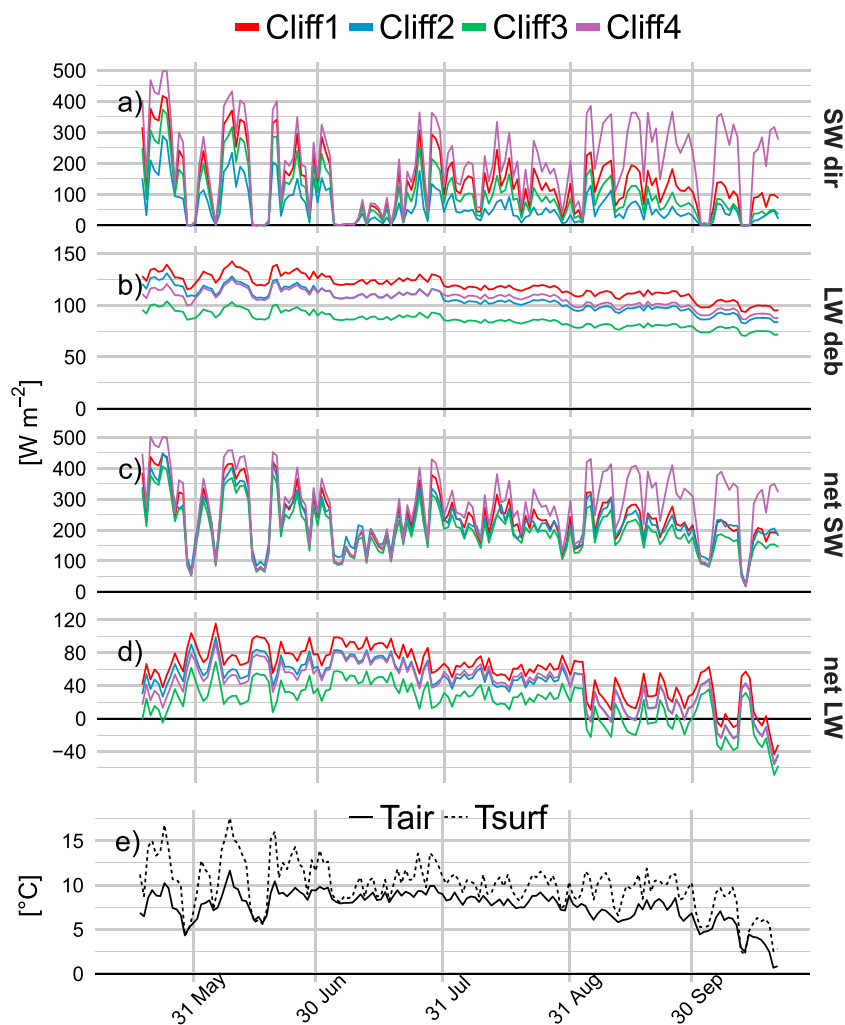
Figure 9. Daily mean values of (a–d) modeled (D Model) radiative fluxes (W m^{-2}) averaged over each cliff and (e) measured temperatures (°C) at AWS Lirung. SW dir, direct shortwave radiation; LW deb, longwave radiation coming from surrounding debris; net SW and net LW, net shortwave and longwave radiation (incoming minus outgoing flux). For shortwave fluxes only the hours between 8:00 and 17:00 (in Nepal Time, UTC +5:45) were considered.

is simulated by the D Model in a satisfying manner (Figure 8), even though the overall deviation in average slope is, at −2.8°.

The overall backwasting of the cliff is reproduced well, with very high agreement at the cliff top and good agreement at the (steep) central basal part (Figure 8c). However, discrepancies are evident at the sides, where the ice-debris boundary does not backwaste enough in the model. Both the eastern and western marginal portions of the cliff are preserved in shape by the D Model, but observations show that they shrank and migrated farther south (Figure 8c). The model thus results in an overestimation of area. These effects are more pronounced in the S Model simulations (Figure 8d), which overestimate the ice cliff surface considerably at the margins but also in the region along the cliff base. The simulated dimensions (D Model) exhibit the highest discrepancies to the observations of the four cliffs (23.2% for the vertical and 18.5% for the horizontal dimension) because of the errors at the margins. The difference in modeled (D Model) and observed mean aspect is instead very small (2.7°, Table 3), because the bulk of the cliff geometry is preserved.

5.1.4. Cliff 4

The most striking characteristic in the evolution of Cliff 4 was its radial growth from May to October (Figure 3), and the D Model reproduces this pattern correctly in its basic dynamics (Figure 8c). The deviations in vertical and horizontal dimensions are low compared to the observed shape (0.1 and 2.1 m, respectively, Table 3). The final simulated outline shows in its southern part a shape congruent to the orthoimage, but a shift eastward
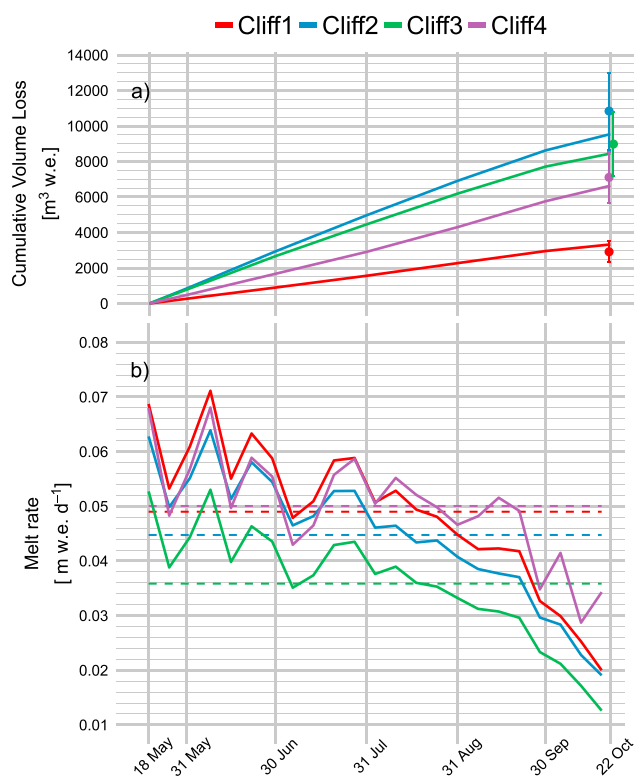
Figure 10. (a) Modeled cliff volume losses from May to October shown as lines, compared to the TIN-generated volume losses (points) with their error bar of $\pm$20%, as estimated in *Brun et al.* [2016]. (b) Modeled daily melt rates (solid lines), averaged per cliff and obtained as the weekly average, and May to October mean cliff melt rates per cliff (dashed lines).

can be recognized. In addition, the elongated dent pointing to the west that is evident in the observations in May is maintained by the model during the cliff backwasting, whereas it disappears in reality (Figure 8c), likely reburied by debris.

The overall slope simulated by the D Model deviates by $-1.8°$ from the observation, the average aspect by $17.4°$ toward west. Another failure of the model is in the steeply sloped lower section of the cliff (section 3) which the model cannot replicate.

5.2. Radiative Fluxes

Cliff 4 receives the highest amount of direct (SW dir, Figure 9) and net (net SW) shortwave radiation of all cliffs throughout the melt season and in particular in September and October. In this period, the direct solar radiation received by Cliff 4 is more than double the amount for Cliffs 1 to 3. This distinct pattern is also evident in the net shortwave radiation. Differences in longwave radiation from the surrounding debris (LW deb) and the total net longwave income (net LW) are less pronounced but still important. Cliff 1 receives the highest longwave radiation throughout the simulation period, and Cliff 3 the lowest. This can be explained by the debris slopes facing Cliff 1 at close distance, as indicated by high debris view factors in Figure 7 (0.35 on average). In contrast, Cliff 3 sees a smaller portion of surrounding debris (0.26 on average).

In general, all fluxes in Figure 9 show a reduced temporal variability during monsoon season (mid-June to beginning of September). Measured air and surface temperatures are also reduced in their variability during this period and differ less compared to premonsoon and postmonsoon.

5.3. Volume Loss, Melt Rate, and Area

Simulated volume losses and melt rates from May to October 2013 calculated with the D Model are shown in Figure 10 and Table 4. Model results are compared to the volume losses derived from high-resolution cliff geometry obtained with SfM as TIN in *Brun et al.* [2016]. Note that the TIN results of *Brun et al.* [2016] are provided as volume of ice but were modified to m^3 w.e. (water equivalent) for comparison, using an assumed ice density of 900 kg m^{-3}. The cliff outlines in premonsoon and postmonsoon which serve as base for the TIN-generated volume losses [*Brun et al.*, 2016] are slightly different from the manually delineated cliffs.

Table 4. Ice Cliff Volume Loss (m³ w.e.) and Mean Backwasting Rate (m w.e. d⁻¹) From May to October 2013 for the Four Cliffs[a]

| | Volume Loss (m³ w.e.) | | | Melt Rate (m w.e. d⁻¹) |
Cliff #	Obs.	Mod.	(%) Dev.	Mod.
1	2,917.3 (2,333.8–3,500.8)	3,325.6	14.0	0.048
2	10,845.1 (8,676.1–13,014.1)	9,544.4	−12.0	0.040
3	8,987.0 (7,189.6–10,784.4)	8,447.6	−6.0	0.033
4	7,110.4 (5,688.3–8,532.5)	6,634.9	−6.7	0.051

[a]Modeled volume losses (Mod., D Model) are compared to the TIN-derived (Obs., based on *Brun et al.* [2016]) volume loss, together with the relative deviation (Dev.) between the modeled and observed values. The uncertainty range of ±20% estimated in *Brun et al.* [2016] is indicated in parentheses. Mean backwasting rates obtained as volume loss divided by the corresponding area are also provided.

Therefore, the volume losses from the TIN approach should be used as a reference rather than an exact validation. The uncertainty range of ±20% estimated in *Brun et al.* [2016] is also indicated in Figure 10a.

Simulated volume losses all agree with the TIN-derived values within the given uncertainty ranges (Figure 10a and Table 4). Estimated volume losses are smaller than the ones of *Brun et al.* [2016] for all cliffs except Cliff 1 (Table 4).

Volume losses at the end of the study period are an integrated variable of cliff backwasting processes. The daily melt rates averaged over the entire cliff area and to weekly values, calculated as melt amount multiplied with inclined area per cell, provide a better insight into temporal patterns of changes (Figure 10b).

The melt rates at all four cliffs show a clear reduction toward the end of the melt season with distinctly lower values in postmonsoon. Melt rates at Cliffs 1, 2, and 4 are similar in magnitude until end of July, when melt at Cliff 4 becomes higher while it decreases at Cliff 2. The melt rate at Cliff 3 is remarkably smaller in magnitude (0.036 m w.e. d⁻¹ on average with a minimum daily melt rate among all cliffs of 0.013 m w.e. d⁻¹ by mid-October), indicating that the high volume losses at this cliff (Figure 10a) is due to the larger area.

The highest melt rate is at Cliff 1 (0.071 m w.e. d⁻¹) in early June before monsoon starts, but this cliff also shows the highest variability during the melt season (0.051 m w.e.) as its melt rate goes down to 0.02 m w.e. d⁻¹. The highest mean melt rate over the entire period of record (May to October) is simulated for Cliff 4, with multiple postmonsoonal increases in melt rate (probably related to the exposure of west oriented cliff sections), whereas melt rates at the other cliffs decrease progressively from mid-September on. This behavior of Cliff 4 results in the lowest variability in melt rate (0.039 m w.e. d⁻¹) among all cliffs.

From Figures 8c and 8d, it is apparent that the model overestimates the cliff area. Comparison of areas per se is not entirely meaningful, as the same total area could result from combination of erroneous cells identified as cliffs together with cliff cells wrongly identified as noncliff. For this reason, we use more sophisticated validation metrics calculated for the projected area that account for the correctly identified cells (section 4.2). Table 2 shows that the D Model reference run has, on average over all four cliffs, a high Recall value (0.872), acceptable precision (0.600), and a high *F* score (0.708). The latter is higher than in all other runs tested.

5.4. Model Sensitivity

The D Model run has the highest average *F* score value of all models (Table 2), which suggests that the chosen parameter values are an appropriate set. The S Model has the lowest value over the four investigated cliffs, confirming the poor performance of this model version (Figures 4 and 8d). The cliff where the D Model performance is worst in terms of Recall rate and *F* score relative to the S Model is Cliff 4. This can be seen in Figure 8d, where the shift of the D Model outline toward east is apparent, which reduces prediction of observed cliff area and therefore lowers the Recall value. In turn, the precision is higher than with the S Model. Ignoring the effect of ponds adjacent to a cliff only slightly decreases the *F* score value, as the main effect of a pond is on the cliff's slope distribution rather than area.

In general, all additional runs have a higher Recall than the D Model reference run (0.872), except for the S Model run and run "rs+20 cm" (with a spatial resolution of 80 cm) and run "$\beta_T - 20\%$" (with a slope threshold of

32°), but very few a higher precision (Table 2). As a result, none of the additional runs has a higher *F* score than the reference run (0.708) except for the run with increased emissivity (0.712), which is only slightly higher.

The factor to which the model seems most sensitive, for the explored ranges, is the debris view factor threshold ("V_{d_T}") used to rebury cliff cells that are surrounded by a large area of debris. The change in the *F* score (0.0116 ΔF/% V_{d_T}) is at least 1 order of magnitude higher than the results from all the other runs.

The standard deviations of the scores (values in parentheses in Table 2) among the four cliffs are generally homogenous with only a small total range over all model runs. The standard deviations are highest for Recall (0.128) and lowest for Precision (0.082).

6. Discussion

6.1. Observations of Cliff Evolution

Out of four cliffs for which detailed, high-resolution observations were available, we noted three main patterns of evolution over the course of an ablation season, indicating a large variability that makes generalizations of cliff behavior difficult. It is clear that detailed observations for a longer duration and for a larger sample size of cliffs are needed to shed light with certainty on the principal processes. However, some key results emerge also from the analysis of four cliffs in this study.

The first is the presence and role of supraglacial ponds at the base of a cliff. The presence of supraglacial ponds adjacent to ice cliffs seems to be one of the main factors controlling whether a cliff flattens or is able to preserve a steep face (Figure 11). The pond maintains a steep cliff directly through thermoerosion or subaqueous melt at the pond-cliff interface and indirectly through exposure of the steep sections to increased longwave radiation emitted by the debris surrounding the cliff-pond system. Steep subaqueous ice slopes were observed with use of a sonar transducer on Lirung Glacier in 2013 (unpublished), which identified that maximum pond depth occurred immediately adjacent to the cliff-pond margin. Observations at other study sites have also revealed a steep subaqueous ice face [e.g., *Benn et al.*, 2001], which might not be the case with all pond-cliff systems but seems to be a frequent characteristic.

A second important factor controlling cliffs' growth is related to reburial by debris. In the model this is accounted for in a twofold way, with a threshold slope under which debris-free cells are reburied and by a threshold for the debris view angle. Despite its simplicity, this approach works satisfactorily. From a combination of model results and observations, this effect seems to be important at the cliff margins, and ignoring it will lead to overestimation of cliffs' areas. However, this should not result in major discrepancies in volume losses as these result mainly from melt occurring in the central section of the cliffs, as indicated by the fact that despite the overestimation of cliff areas by the model, the total volume loss is simulated correctly (Figure 10). Nevertheless, for modeling applications aimed at understanding future cliff evolution, inclusion of this aspect seems imperative to avoid unlimited areal growth which would translate into erroneous melt and backwasting patterns over the long term.

Observations also show a variety of aspects and shapes, and while none of the cliffs has a south facing orientation, it is remarkable that the only growing cliff was the west facing Cliff 4, which received much higher average radiative energy than the other three cliffs (Figure 9). We were not able to attribute this growth to aspect alone, but the distributed, high-resolution simulation of the radiative fluxes provides a clear indication of higher energy receipts. This also highlights the importance of a grid-based, sophisticated model of energy fluxes.

6.2. Model Simulations

The dimensions and geometry of the cliffs after one melt season are reproduced by the new model approach (D Model) in an accurate manner. Simulated mean aspect and slope per cliff deviated only by a few degrees from the observations (Table 3). The higher difference in aspect of Cliff 4 (12.8° toward south) is mainly caused by its strong radial expansion from May to October and the resulting generation of a high range of aspects. Modeled vertical and horizontal extents are in close agreement with the observed distances, except for Cliff 3, which shows an overestimation of about 20% along both dimensions. The penetration of its southwest remnant too far into the debris slope caused overestimation of the maximum elevation and thus of the vertical cliff extent, as the lowest cliff section was modeled correctly. The horizontal excess compared to the observations is due to overestimation of areas in both the southwest and east parts of Cliff 3. Cliff 3 is the one for which discrepancies in the geometric characteristics are strongest. Nevertheless, the overall pattern of
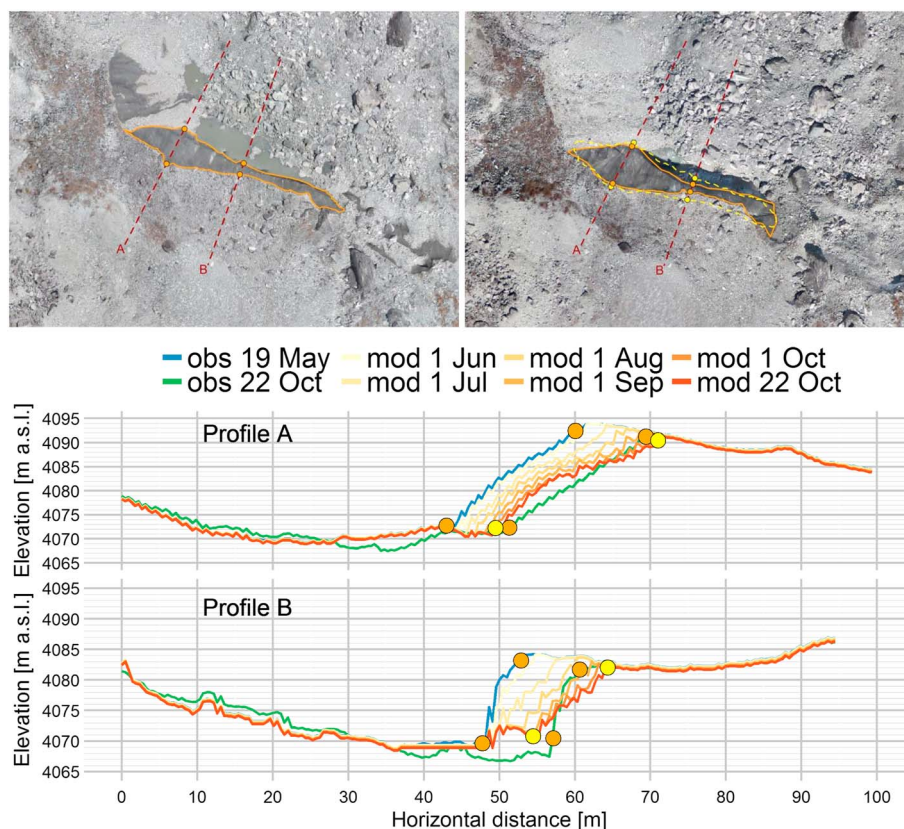
Figure 11. (top) Orthoimages showing the glacier surface in (left) May and (right) October 2013, with observed (orange solid) and modeled (yellow dashed) final Cliff 2 outlines. The corresponding debris-ice contact points are indicated with dots (using the same color scheme: orange for observations and yellow for model results). The two transects A and B (dark red dashed) are also shown. (bottom) Elevation profiles across Cliff 2 as observed in May and October (blue and green) and modeled from May (yellow) to October (red). The dots indicate the interfaces indicated in the orthoimages above (using the same color scheme: orange for observations and yellow for model results).

backwasting in the uppermost section of the cliff is reproduced very well by the model, and total volume losses agree with the observed values (Figure 10). For Cliffs 1, 2, and 4 simulated dimensions, slope and aspect patterns, and maximum elevations all agree well with the UAV observations, suggesting that the overall backwasting pattern is reproduced by the model.

Despite the overall good general agreement (F score >0.7), discrepancies are still evident when comparing the cliffs' outlines and areas. This suggests that additional processes not included in the model may be important or that a better representation of included processes is needed. In particular, the recovering of marginal cliff cells with debris, implemented with a threshold slope and debris view factor, is not entirely reproduced by the model and leads to an overestimation of the cliff area especially for Cliff 3 (Figures 8c and 8d). Examination of the surface topography adjacent to the cliff suggests that more complex sourcing of debris contributes to the reburial of sections of cliffs (Figure 12). Cliff 3 seems to have backwasted prior to the May 2013 observation along a relatively steep and uniformly inclined debris slope, and the debris flank left behind is visible NW of the cliff (white arrows in Figure 12a). However, during the 2013 melting season the cliff recedes farther down, while the model simulates the cliff to follow the ridge and end up in October at its southern front (Figure 12b), similar to the initial position of this cliff's margin in May (Figure 12a). The formation of the debris flank is modeled correctly, but the reburial of the ice surface is not. Inspection of the topography of the debris slopes shows concave crests surrounding the cliff western margin (Figure 12c) that are likely to contribute additional debris. This, coming from the sidewardly concave ridge above the southwestern section of the cliff, accumulated in the small cirque at its base (see Figure 12c), decreasing the local slope and leading to the disappearance of that section of the cliff. The morphometric characteristics of the ridge and its debris supply are difficult to model without adding increasing complexity and specific parameterizations, despite clearly playing a role in controlling the debris presence or removal through gravitational processes.
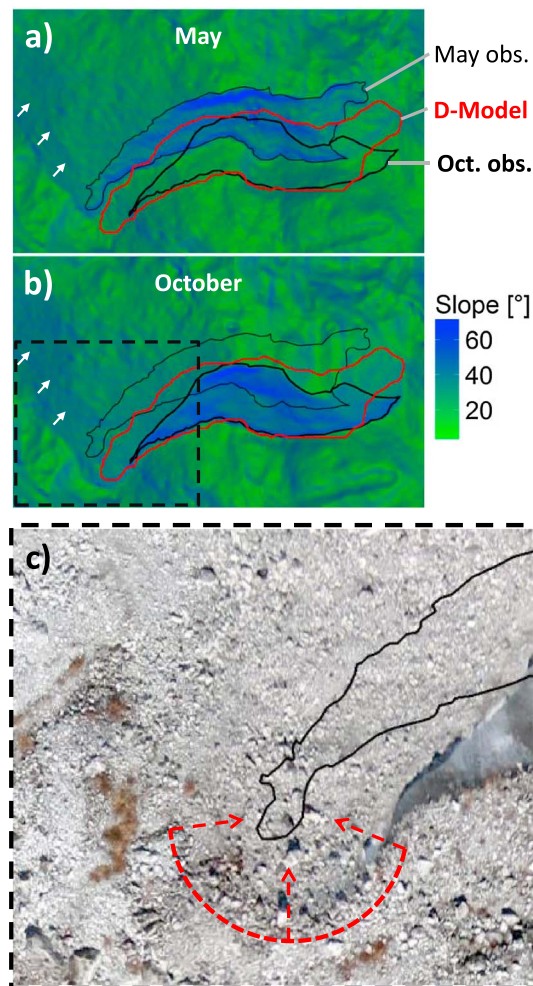
Figure 12. Observed slopes at and around Cliff 3 in (a) May and (b) October are shown in the background. Thin and bold black outlines in the foreground show the observed cliff outlines in May and October, respectively. The red outline is the D Model result. White arrows indicate the ridge and dip direction of the main debris slope as a trace from cliff backwasting path. (c) A reason for the large overestimation of the modeled cliff area could be convergent accumulation of debris in the cirque sourcing from concave crests (red dashed line), which could not be considered in the model.

In general, the environment surrounding the ice cliffs may explain some of the variability in behavior and in transitions between cliff types, as much as the processes acting directly on the ice itself. Cliffs retreating into slopes with the same aspects to the cliff would cause a lowering of the ice cliff (Figure 11), while retreat into a slope with the opposite aspect to the cliff would result in a heightening. The model reproduces these effects well, given the high resolution and quality of the DEM available (Figure 11), suggesting that this effect can be simulated as long as the surrounding topography is correctly represented. However, a mechanism that is not currently included is the effect of varying debris thickness at the top of the cliff. Debris cover thickness varies over short spatial scales, and cliff retreat into a thickening cover at the top of the wall might explain burial of the base. In general, the model simulates the top ridge of the cliffs correctly (especially for Cliffs 1 and 3), but has some problems in predicting the cliff base position (e.g., Cliff 3), which is likely due to convergent accumulation of debris in the cirque close to the cliff (Figure 12). The redistribution of debris from above the ice cliff to its base is only crudely represented in the model by a slope-based control on the area identified as cliff. Physically, the reburial of the base of the cliff and the accumulation of debris mounds depend on the debris thickness above the cliff, retreat rates, and ice cliff slope, all controlling the runout and deposition of small rockfall events.

6.3. Model Limitations

Some of the approaches implemented in the model presented here are simple and could be improved toward more physically based formulations. The effect of an adjacent pond is included through prescription of a constant subaqueous melt rate and an affected area that was defined based on sensitivity tests. A more advanced approach could be devised based on the temperature of the pond water but would require data that are not easily available. Equally, the reburial by debris is parameterized as a function of slope and the amount of debris that is seen by any given cell of the cliff. A more accurate representation could be based on prescription of a source area and debris characteristics, but this also would imply knowledge of the geology of the debris and more burdensome calculations in a model that is already very complex. The main modeling goal that drove the formulation of the model was to incorporate first-order controls of cliff changes in a manner that would allow the model to be run for several cliffs and relatively long times without requiring too detailed or specific data sets.

A more stringent limitation related to the effect of ponds is the lack of knowledge about their hydrological variability and water levels. The reversal of slope observed at Cliff 4, with a flat lower cliff section in May turning into a steep one in October, was not reproduced by the model but could be explained by varying pond levels, which are not considered in the simulations. According to observations, the pond adjacent to Cliff 4 lowered substantially toward postmonsoon, exposing a newly steep section at the cliff base, where the pond most probably filled up in early premonsoon flooding the lower cliff zone.

The partial disagreement between the observations and modeled cliff geometry for Cliffs 1 and 3 might also be explained by the fact that between the two field visits of May and October 2013 the boundary conditions in the immediate vicinity of the cliffs changed significantly, most likely by the appearance of an ephemeral pond. In general, observations during monsoon and knowledge about pond evolution on debris-covered glaciers are very limited [*Watson et al.*, 2016]. Therefore, it is difficult to make assumptions about potential interseasonal occurrence of supraglacial ponds and prescribe variable pond levels in the model. Nevertheless, it is evident that comparison of model results with field observations can provide insights into processes occurring in the time between observations.

Another model limitation is related to some of the meteorological input data, which were applied in a nondistributed way: unlike the radiative fluxes, air temperature, relative humidity, and wind speed were assumed to be uniform in space. The point-scale AWS measurements were taken as such and uniformly applied to each cliff cell, because of lack of better methods for their extrapolation or modeling. Investigations into the micrometeorology of high-elevation debris-covered tongues and Himalayan glaciers is, despite recent progress [e.g., *Steiner and Pellicciotti*, 2016; *Collier and Immerzeel*, 2015], a field still in need of sustained focus.

Surface parameters (surface roughness, and ice and debris albedo) were also assumed uniform in space. Despite the fact that they can show high spatial and temporal variability, these quantities are difficult to measure in a distributed manner at the cliff scale, for obvious logistic difficulties. Debris albedo depends on radiation patterns and shadow, precipitation determining the wetness of the surface, and debris properties. Ice reflectance additionally depends on preferential melt flow paths and amount of debris sources above the cliff as well as refreezing. Very little is known about surface roughness of cliffs and debris surfaces in general [*Brock et al.*, 2010; *Rounce et al.*, 2015]. For both albedo and surface roughness we used values optimized in *Steiner et al.* [2015] for Cliffs 1 and 2 where comprehensive survey data sets were available in both premonsoon and postmonsoon 2013, but it is clear that a better understanding of the spatial and temporal variability of cliff surface properties could lead to improvements in modeling outputs.

The model seems to have problems in handling very thin, branching cliff segments, as could be seen in the modeled outlines of Cliff 4. This could lead to the development of incorrect cliff remnants with the wrong aspect, a problem that was small for Cliff 4 but could be more significant for other cliffs. As noted above, discrepancies in cliff areas would not necessary result in large errors in simulated volume losses as long as the areas are marginal, but depending on their main aspect they could represent a source of error over the long period.

6.4. Comparison With Other Studies

Despite apparent recent advances, models of cliff backwasting are still in their infancy. The three main works that have presented backwasting models [*Sakai et al.*, 1998; *Han et al.*, 2010; *Reid and Brock*, 2014] are all point-scale models that only take into account the effect of atmospheric energy on cliff ablation.

The development of the first grid-based model of cliff ablation that considered the cliff surface as a 3-D domain was a significant step forward [*Buri et al.*, 2016]. This work shed considerable light on the spatial variability over a single cliff of the atmospheric forcing and quantified for the first time the relative importance of the various fluxes. However, that model includes only the atmospheric forcing (although in a distributed manner) and does not consider other processes that modulate the backwasting of a cliff and its geometrical changes. Here we show that updating the surface geometry is crucial for realistic calculations of the volume lost by a cliff during one ablation season and that a gridded representation of the cliff surface is necessary to quantify melt rates appropriately. We also show that accounting for melt at the surface of the cliff exposed to the atmosphere is only one of the processes that drive the dynamics of cliffs and their survival and decay.

Simulations with the new model provide an estimate of May–October mass losses from the four cliffs investigated that range from 3326 (Cliff 1) to 9544 (Cliff 2) m^3 w.e. The contribution of the four cliffs to total subdebris melt, estimated with an advanced glaciohydrological model [*Ragettli et al.*, 2015], is 3.25%. This value is remarkable, given the small area ice cliffs cover relative to total debris-covered area (0.19%).

In a recent study on Ngozumpa Glacier, Everest region, *Thompson et al.* [2016] found that cliffs accounted for 40% of the volume losses over the stagnant portion of the glacier tongue by differencing of DEMs. It is difficult to compare these values to those obtained in our study, because the method used by *Thompson et al.* [2016] often also included ponds in the area regarded as cliff, leading to high uncertainty. It would be useful to apply our model to all cliffs over a large glacier and compare those estimates to those of *Thompson et al.* [2016].

The new model could also be used to understand long-term patterns of cliff changes over several ablation seasons and employed to test hypotheses on cliffs survivals such as that only north facing cliffs (on the Northern Hemisphere) survive over multiple seasons that have been put forward but never demonstrated.

The model, however, given the level of complexity and physical detail included, might not be applicable as such at the glacier scale, for computational reasons and because it requires high-resolution DEMs of the cliffs and their surrounding topography that are rarely available for an entire glacier or catchment. For applications at this spatial scale, for which only coarser-resolution DEMs are generally available, the effect of the DEM resolution on the accuracy of the model outputs needs to be tested.

7. Conclusions

In this paper, we have used a new data set of high-resolution observations of cliff evolution over one ablation season to identify patterns of changes over four cliffs on the debris-covered tongue of Lirung Glacier. The four cliffs have different shape, dominant orientation and slopes, and different degree and history of coupling to a supraglacial pond. We use the observations to infer the dominant processes controlling the observed evolution based on analysis of backwasting rates and cliffs' geometrical properties. We then use the knowledge gained in this way to develop a model of cliff backwasting that takes existing models a step forward by including the cliffs dynamics in response to atmospheric forcing (included to date), the effect of ponds at the cliff base, and reburial by debris. To our knowledge, this is the first model to move beyond theoretical ablation rates for an invariant surface and to represent 3-D evolution of cliffs.

Our main conclusions are as follows:

1. Out of four investigated cliffs, three different and contrasting patterns of evolution are evident. We show that cliffs on the same glacier and at short distance within each other can both flatten and recline, remain remarkably self-similar during one ablation season, or expand radially in a considerable manner.
2. We were able to identify some of the mechanisms controlling the patterns described above through a combination of high-resolution observations and an advanced model. In particular, we developed a model that accounts for the three main processes that seem to be first-order controls on cliff evolution: (i) atmospheric melt, (ii) pond contact ablation enhancement for the cliff base, and (iii) reburial by surrounding debris.
3. The modeling approach suggested is able to simulate the cliff evolution over one melt season in a satisfying way in terms of horizontal and vertical extent as well as mean slope and aspect. The model simulates the progressive backwasting through interaction with the surrounding topography, allowing the cliff shape to grow and to shrink over time. While there is room for further refinement, the model is able to capture the main cliff dynamics and geometric transformation. Importantly, the model application has clearly shown that for very high resolution studies, neglecting a dynamic update of the cliff geometry would lead to

erroneous results in terms of backwasting patterns and volumes. Similarly, ignoring the effect of adjacent ponds or reburial by debris misses major factors affecting cliff evolution

4. Observations and model results suggest a strong dependency of the cliffs' life cycle on supraglacial ponds, as the water body keeps the cliff geometry constant through a combination of subaqueous and atmospheric backwasting as well as calving at the base to maintain steep ice cliff slopes in the lowest sections. The absence of ponds causes the progressive flattening of the cliff, which finally leads to complete disappearance.

Despite the clear advances, several improvements are still possible and require high-resolution time series data sets of cliff geometry, coupled to pond changes and an understanding of debris local motion, sourcing, and redistribution. This calls for increased monitoring efforts from high-resolution imagery and field observations to collect a larger sample of cliffs to categorize cliff behavior based on the insights provided here. These should encompass a variety of sites (others in the Himalaya and in other regions of the world), greater number of cliffs, and a longer duration (e.g., evolution over several years).

References

Benn, D., S. Wiseman, and K. Hands (2001), Growth and drainage of supraglacial lakes on debris-mantled Ngozumpa Glacier, Khumbu Himal, Nepal, *J. Glaciol.*, *47*(159), 626–638.

Benn, D. I., T. Bolch, K. Hands, J. Gulley, A. Luckman, L. I. Nicholson, D. Quincey, S. Thompson, R. Toumi, and S. Wiseman (2012), Response of debris-covered glaciers in the Mount Everest region to recent warming, and implications for outburst flood hazards, *Earth-Sci. Rev.*, *114*(1–2), 156–174, doi:10.1016/j.earscirev.2012.03.008.

Bivand, R. S., E. Pebesma, and V. Gomez-Rubio (2013), *Applied Spatial Data Analysis With R*, 2nd edn., Springer, New York.

Bolch, T., et al. (2012), The state and fate of Himalayan glaciers, *Science*, *336*(6079), 310–314, doi:10.1126/science.1215828.

Brock, B. W., C. Mihalcea, M. P. Kirkbride, G. Diolaiuti, M. E. J. Cutler, and C. Smiraglia (2010), Meteorology and surface energy fluxes in the 2005–2007 ablation seasons at the Miage debris-covered glacier, Mont Blanc Massif, Italian Alps, *J. Geophys. Res.*, *115*, D09106, doi:10.1029/2009JD013224.

Brun, F., P. Buri, E. S. Miles, P. Wagnon, J. F. Steiner, E. Berthier, S. Ragettli, P. Kraaijenbrink, W. W. Immerzeel, and F. Pellicciotti (2016), Quantifying volume loss from ice cliffs on debris-covered glaciers using high-resolution terrestrial and aerial photogrammetry, *J. Glaciol.*, *62*, 684–695, doi:10.1017/jog.2016.54.

Buri, P., F. Pellicciotti, J. F. Steiner, E. S. Miles, and W. W. Immerzeel (2016), A grid-based model of backwasting of supraglacial ice cliffs on debris-covered glaciers, *Ann. Glaciol.*, *57*(71), 199–211, doi:10.3189/2016AoG71A059.

Cogley, J. G. (2016), Glacier shrinkage across High Mountain Asia, *Ann. Glaciol.*, *57*(71), 41–49, doi:10.3189/2016aog71a040.

Collier, E., and W. W. Immerzeel (2015), High-resolution modeling of atmospheric dynamics in the Nepalese Himalaya, *J. Geophys. Res. Atmos.*, *120*(19), 9882–9896, doi:10.1002/2015JD023266.

Dice, L. R. (1945), Measures of the amount of ecologic association between species, *Ecology*, *26*(3), 297–302, doi:10.2307/1932409.

Dong, J., and C. Peters-Lidard (2010), On the relationship between temperature and MODIS snow cover retrieval errors in the western U.S., *IEEE J. Sel. Topics Appl. Earth Obs. Remote Sens.*, *3*(1), 132–140, doi:10.1109/jstars.2009.2039698.

Driscoll, F. G. (1980), Wastage of the Klutlan ice-cored moraines, Yukon Territory, Canada, *Quat. Res.*, *14*(1), 31–49.

Edelsbrunner, H., D. Kirkpatrick, and R. Seidel (2006), On the shape of a set of points in the plane, *IEEE Trans. Inf. Theor.*, *29*(4), 551–559, doi:10.1109/TIT.1983.1056714.

Evatt, G. W., I. D. Abrahams, M. Heil, C. Mayer, J. Kingslake, S. L. Mitchell, A. C. Fowler, and C. D. Clark (2015), Glacial melt under a porous debris layer, *J. Glaciol.*, *61*(229), 825–836, doi:10.3189/2015jog14j235.

Foster, L. (2010), Utilisation of remote sensing for the study of debris-covered glaciers: Development and testing of techniques on Miage Glacier, Italian Alps., Phd thesis, Univ. of Dundee.

Gardelle, J., E. Berthier, and Y. Arnaud (2012), Slight mass gain of Karakoram glaciers in the early twenty-first century, *Nature Geosci*, *5*(5), 322–325, doi:10.1038/ngeo1450.

Gardelle, J., E. Berthier, Y. Arnaud, and A. Kääb (2013), Region-wide glacier mass balances over the Pamir-Karakoram-Himalaya during 1999–2011, *The Cryosphere*, *7*(4), 1263–1286, doi:10.5194/tc-7-1263-2013.

Gilani, S. Z., and N. I. Rao (2009), A clustering based automated glacier segmentation scheme using digital elevation model, in *Proceedings of the Digital Image Computing: Techniques and Applications, 2009. DICTA'09.*, pp. 277–284, IEEE Computer Society, Washington, D. C.

Han, H., J. Wang, J. Wei, and S. Liu (2010), Backwasting rate on debris-covered Koxkar glacier, Tuomuer mountain, China, *J. Glaciol.*, *56*(196), 287–296, doi:10.3189/002214310791968430.

Herreid, S., F. Pellicciotti, A. Ayala, A. Chesnokova, C. Kienholz, J. Shea, and A. Shrestha (2015), Satellite observations show no net change in the percentage of supraglacial debris-covered area in northern Pakistan from 1977 to 2014, *J. Glaciol.*, *61*(227), 524–536, doi:10.3189/2015jog14j227.

Hijmans, R. J. (2015), Raster: Geographic data analysis and modeling, *R package version 2.4-20*, *2*, 15.

Horn, B. K. (1981), Hill shading and the reflectance map, *Proc. IEEE*, *69*(1), 14–47, doi:10.1109/PROC.1981.11918.

Immerzeel, W., P. Kraaijenbrink, J. Shea, A. Shrestha, F. Pellicciotti, M. Bierkens, and S. de Jong (2014), High-resolution monitoring of Himalayan glacier dynamics using unmanned aerial vehicles, *Remote Sens. Environ.*, *150*, 93–103, doi:10.1016/j.rse.2014.04.025.

Inoue, J., and M. Yoshida (1980), Ablation and heat exchange over the Khumbu Glacier, *J. Jpn. Soc. Snow Ice*, *41*, 26–33, doi:10.5331/seppyo.41.Special_26.

Iwata, S., O. Watanabe, and H. Fushimi (1980), Surface morphology in the ablation area of the Khumbu Glacier, *J. Jpn. Soc. Snow Ice*, *41*(Special), 9–17, doi:10.5331/seppyo.41.Special_9.

Kääb, A., E. Berthier, C. Nuth, J. Gardelle, and Y. Arnaud (2012), Contrasting patterns of early twenty-first-century glacier mass change in the Himalayas, *Nature*, *488*(7412), 495–498, doi:10.1038/nature11324.

Kirkbride, M. P., and P. Deline (2013), The formation of supraglacial debris covers by primary dispersal from transverse englacial debris bands, *Earth Surf. Process. Landforms*, *38*(15), 1779–1792, doi:10.1002/esp.3416.

Miles, E. S., I. Willis, F. Pellicciotti, J. F. Steiner, P. Buri, and N. Arnold (2016), Refined energy-balance modelling of a supraglacial pond, Langtang Khola, Nepal, *Ann. Glaciol.*, *57*(71), 29–40, doi:10.3189/2016AoG71A421.

Nicholson, L., and D. I. Benn (2006), Calculating ice melt beneath a debris layer using meteorological data, *J. Glaciol.*, *52*(178), 463–470.

Olson, D. L., and D. Delen (2008), *Advanced Data Mining Techniques*, Springer Science + Business Media, Berlin.

Østrem, G (1959), Ice melting under a thin layer of moraine, and the existence of ice cores in moraine ridges, *Geografiska Annaler*, *41*(4), 228–230.

Pellicciotti, F., C. Stephan, E. Miles, S. Herreid, W. Immerzeel, and T. Bolch (2015), Mass-balance changes of the debris-covered glaciers in the Langtang Himal, Nepal, 1974–1999, *J. Glaciol.*, *61*(226), 373–386, doi:10.3189/2015JoG13J237.

Pickard, J. (1983), Short notes: Surface lowering of ice-cored moraine by wandering lakes, *J. Glaciol.*, *29*(102), 338–342.

Purdie, J., and B. Fitzharris (1999), Processes and rates of ice loss at the terminus of Tasman Glacier, New Zealand, *Global Planet. Change*, *22*(1–4), 79–91, doi:10.1016/S0921-8181(99)00027-2.

Core Team, R (2015), *R: A Language and Environment for Statistical Computing*, R Foundation for Statistical Computing, Vienna, Austria.

Ragettli, S., F. Pellicciotti, W. W. Immerzeel, E. S. Miles, L. Petersen, M. Heynen, J. M. Shea, D. Stumm, S. Joshi, and A. Shrestha (2015), Unraveling the hydrology of a Himalayan catchment through integration of high resolution in situ data and remote sensing with an advanced simulation model, *Adv. Water Resour.*, *78*, 94–111, doi:10.1016/j.advwatres.2015.01.013.

Ragettli, S., T. Bolch, and F. Pellicciotti (2016), Heterogeneous glacier thinning patterns over the last 40 years in Langtang Himal, Nepal, *The Cryosphere*, *10*(5), 2075–2097, doi:10.5194/tc-10-2075-2016.

Reid, T., and B. Brock (2014), Assessing ice-cliff backwasting and its contribution to total ablation of debris-covered Miage glacier, Mont Blanc massif, Italy, *J. Glaciol.*, *60*(219), 3–13, doi:10.3189/2014JoG13J045.

Rittger, K., T. H. Painter, and J. Dozier (2013), Assessment of methods for mapping snow cover from MODIS, *Adv. Water Resour.*, *51*, 367–380, doi:10.1016/j.advwatres.2012.03.002.

Röhl, K. (2008), Characteristics and evolution of supraglacial ponds on debris-covered Tasman Glacier, New Zealand, *J. Glaciol.*, *54*(188), 867–880.

Rounce, D. R., D. J. Quincey, and D. C. McKinney (2015), Debris-covered glacier energy balance model for Imja–Lhotse Shar Glacier in the Everest region of Nepal, *The Cryosphere*, *9*(6), 2295–2310, doi:10.5194/tc-9-2295-2015.

Sakai, A., M. Nakawo, and K. Fujita (1998), Melt rate of ice cliffs on the Lirung glacier, Nepal Himalayas, 1996, *Bull. Glacier Res.*, *16*, 57–66.

Sakai, A., N. Takeuchi, K. Fujita, and M. Nakawo (2000), Role of supraglacial ponds in the ablation process of a debris-covered glacier in the Nepal Himalayas, *IAHS Publ.*, *265*, 119–132.

Sakai, A., K. Nishimura, T. Kadota, and N. Takeuchi (2009), Onset of calving at supraglacial lakes on debris-covered glaciers of the Nepal Himalaya, *J. Glaciol.*, *55*(193), 909–917, doi:10.3189/002214309790152555.

Scherler, D., B. Bookhagen, and M. Strecker (2011), Spatially variable response of Himalayan glaciers to climate change affected by debris cover, *Nat. Geosci.*, *4*(3), 156–159, doi:10.1038/ngeo1068.

Steiner, J., F. Pellicciotti, P. Buri, E. Miles, W. Immerzeel, and T. Reid (2015), Modeling ice cliff backwasting on a debris covered glacier in the Nepalese Himalayas, *J. Glaciol.*, *61*(229), 889–907, doi:10.3189/2015JoG14J194.

Steiner, J. F., and F. Pellicciotti (2016), Variability of air temperature over a debris-covered glacier in the Nepalese Himalaya, *Ann. Glaciol.*, *57*(71), 295–307, doi:10.3189/2016aog71a066.

Tachikawa, T., M. Hato, M. Kaku, and A. Iwasaki (2011), Characteristics of ASTER GDEM version 2, in *2011 IEEE International Geoscience and Remote Sensing Symposium*, pp. 3657–3660, IEEE, Vancouver, B. C., doi:10.1109/igarss.2011.6050017

Thompson, S., D. I. Benn, J. Mertes, and A. Luckman (2016), Stagnation and mass loss on a Himalayan debris-covered glacier: Processes, patterns and rates, *J. Glaciol.*, *62*(233), 467–485, doi:10.1017/jog.2016.37.

Watson, C. S., D. J. Quincey, J. L. Carrivick, and M. W. Smith (2016), The dynamics of supraglacial ponds in the Everest region, central Himalaya, *Global Planet. Change*, *142*, 14–27, doi:10.1016/j.gloplacha.2016.04.008.

Watson, R. (1980), Landform development on moraines of the Klutlan Glacier, Yukon Territory, Canada, *Quaternary Res.*, *14*(1), 50–59.

Wickham, H. (2009), *GGPLOT2: Elegant Graphics for Data Analysis*, Springer, New York.

Zou, K. H., S. K. Warfield, A. Bharatha, C. M. Tempany, M. R. Kaus, S. J. Haker, W. M. Wells, F. A. Jolesz, and R. Kikinis (2004), Statistical validation of image segmentation quality based on a spatial overlap index, *Acad. Radiol.*, *11*(2), 178–189, doi:10.1016/s1076-6332(03)00671-8.